Capillarity

Vol. 4, No. 3, p. 50-62, 2021

Original article

Numerical study of the effect of tortuosity and mixed wettability on spontaneous imbibition in heterogeneous porous media

Zhenhan Diao[1], Sheng Li[1], Wei Liu[2], Haihu Liu[1]*, Qingfeng Xia[3]

[1]*School of Energy and Power Engineering, Xi'an Jiaotong University, Xi'an 710049, P. R. China*

[2]*Department of Mechanical Engineering, National University of Singapore, 10 Kent Ridge Crescent, Singapore 119260*

[3]*Huawei Technology Co. Ltd., Shenzhen 518129, P. R. China*

Keywords:
Spontaneous imbibition
tortuosity
mixed wettability
quasi-3D simulation
heterogeneous micromodel

Cited as:
Diao, Z., Li, S., Liu, W., Liu, H., Xia, Q. Numerical study of the effect of tortuosity and mixed wettability on spontaneous imbibition in heterogeneous porous media. Capillarity, 2021, 4(3): 50-62, doi: 10.46690/capi.2021.03.02

Abstract:
Spontaneous imbibition in porous media plays an important role in numerous industrial processes, but its underlying mechanisms are still poorly understood due to the complicated structure and multiple surface properties of natural porous media. In order to fill this gap, a quasi-three-dimensional color-gradient lattice Boltzmann model is applied to simulate the spontaneous imbibition in heterogeneous porous media micromodels, where the influence of viscosity ratio, tortuosity and mixed wettability is systematically investigated. Results show that the tortuosity has less influence on imbibition than the viscosity ratio, which leads to unstable displacement for viscosity ratios smaller than unity and to stable displacement for viscosity ratios greater than unity. By establishing the power-law relationship between wetting fluid saturation and time, it is found that the scaling exponent is not only affected by tortuosity, but also related to pore throat structure of the micromodel. In addition, the mixed wettability is found to significantly influence the stability of displacement, especially when the contact angle difference of two constituents is large. Specifically, the greater the mixing degree of two wettabilities, the more unstable the displacement will become, which results in an enhanced interface roughening. Accordingly, the scaling exponent deviates more from the prediction from the Lucas-Washburn equation. Due to the reduced connectivity of flow paths, the wetting fluid imbibition rate in mixed wettability condition is lower than that in uniform wettability condition, no matter whether the latter theoretically corresponds to a slow displacement or not.

1. Introduction

The spontaneous imbibition in porous media refers to a process that the wetting fluid is spontaneously drawn into void space under the effect of capillary pressure, and it plays a significant role in numerous industrial and technological applications, such as paper sensors (Elizalde et al., 2015), carbon dioxide sequestration (Guo et al., 2016), oil and gas extraction (Gao et al., 2018; Liu et al., 2019) and inkjet printing (Wijshoff, 2018). Particularly, the spontaneous imbibition is one of the most important mechanisms to enhance oil recovery in tight reservoirs (You et al., 2018; Ahmadi et al., 2020). Therefore, much effort has been devoted to investigate the spontaneous imbibition within porous media and its underlying mechanism (Gao and Hu, 2018; Bartels et al., 2019; Andersen et al., 2020). However, due to the complicated structure of porous media and numerous factors influencing the fluid flow, e.g., the wettability of porous medium (Graue and Ferno, 2011), surface roughness (Espin and Kumar, 2015), initial water saturation (Gao and Hu, 2016), pore structure

Yandy Scientific Press

*Corresponding author.
E-mail address: 3120103194@stu.xjtu.edu.cn (Z. Diao); lisheng6@stu.xjtu.edu.cn (S, Li); liuwei09@u.nus.edu (W. Liu); haihu.liu@mail.xjtu.edu.cn (H. Liu); xiaqingfeng1@huawei.com (Q. Xia).

Received July 7, 2021; revised July 16, 2021; accepted July 20, 2021; available online July 24, 2021.

(Zacharoudiou et al., 2017), and the gravity (Wang and Cheng, 2020; Li et al., 2021), the dynamics of spontaneous imbibition in porous media, especially in heterogeneous porous media, remains poorly understood, which limits the development of strategies to optimize its applications.

The research of spontaneous imbibition can be traced back to the pioneering works of Lucas (1918) and Washburn (1921), who focused on negligible viscosity of non-wetting fluid and derived the classic Lucas-Washburn (LW) equation describing the relationship between imbibition length l and imbibition time t, i.e., $l \propto \sqrt{t}$. Later, it was reported that the LW equation analytically derived from a single capillary tube can be extended to describe the spontaneous imbibition in homogeneous porous media (Gruener and Huber, 2011; Gruener et al., 2012). Nevertheless, some studies have found that this equation is not applicable when the pore structure of porous media is relatively complex (Karoglou et al., 2005; Bru and Pastor, 2006; Hu et al., 2012; Yang et al., 2016; Chang et al., 2018). On the other hand, the LW equation has been modified to account for the effects of tortuosity and mixed wettability, but these studies are limited to simple geometries, such as a single tortuous capillary (Cai et al., 2010) and mixed-wet pores (Wang et al., 2020). Therefore, the research of spontaneous imbibition in heterogeneous porous media with varying tortuosity and/or mixed wettability from a pore-scale viewpoint is essential, which enables us to clarify which existing scaling laws (e.g., the LW equation) are valid and even construct new scaling or constitutive equations for macroscopic scales.

The spontaneous imbibition in porous medium with different tortuosities or mixed wettabilities has been studied in recent years. Cai et al. (2012) derived an analytical model which includes gravity for characterizing spontaneous imbibition of wetting liquid vertically into gas-saturated porous media, and they found that the weight of wetting liquid imbibed into porous media is a function of tortuosity. Shi et al. (2017) conducted gas migration experiments in mixed wetting bead models initially saturated with water, and their results indicated that the likelihood of gas migration driven by buoyancy increases in a logarithmic form with increasing the fraction of oil-wetting grains. Zheng et al. (2018) quantitively investigated the influence of tortuosity, channel shape on the imbibition behavior and the advancing behavior of competing interfaces in two-dimensional (2D) bifurcated channels by a lattice Boltzmann pseudo-potential model. With the aid of fast X-ray tomography technology, Bartels et al. (2019) found that the formation of a spontaneous imbibition front occurs only in water-wet systems, and mixed-wet systems show localized imbibition events only. By conducting experiments in a low-permeability mixed-wettability rock, Liu et al. (2020) discussed and analyzed the relationships among the contact angle, capillary force, recovery ratio, wettability, and the micro-imbibition recovery.

As reviewed above, previous studies on spontaneous imbibition under different tortuosities mainly focused on the 2D simulations, and they ignored three-dimensional (3D) effects, i.e., the effects of depth on the flow behavior. In spontaneous imbibition simulations, two most important 3D effects need to be considered: (1) the viscous resistance from top and bottom walls, and (2) the interface curvature change due to the confinement of top and bottom walls, which is indispensable to overcome the capillary valve resistance through pore-throat structure (Liu et al., 2021). On the other hand, the previous researches on spontaneous imbibition with mixed wettability almost all rely on experiments, which are costly, time-consuming and involve many uncertainties associated with microfabrication and experimental measurement. Numerical simulations can overcome these limitations, thereby providing more convincing results about spontaneous imbibition in porous media micromodels with controllable mixed wettability.

The purpose of this work is to explore the effects of tortuosity and mixed wettability on spontaneous imbibition in natural porous media with the help of pore-scale simulations. Under the influences of sedimentation, diagenesis and tectonism, the size, shape and distribution of pores and throats, as well as the physical properties such as permeability, tortuosity and wettability in natural porous media present spatial variations (Liu et al., 2018; Gao et al., 2019; Zhu et al., 2020), meaning that the natural porous media is usually heterogeneous. Thus, heterogeneous micromodels will be selected as representatives for the present study. Each micromodel is composed of a 2D heterogeneous pore network having relatively small and uniform depth. Compared to macro-scale simulations, pore-scale simulations can not only provide detailed information on the fluid flows in pores and throats, but also easily capture some important physical phenomena, such as capillary valve effect, preferential flow paths, and so on (Xu et al., 2017). A number of approaches have been developed to simulate multiphase flows at pore scale, which include pore-network models (Joekar-Niasar et al., 2013), lattice Boltzmann method (LBM), smoothed particle hydrodynamics (Bandara et al., 2013; Tartakovsky et al., 2016), and traditional computational-fluid-dynamics-based methods like volume-of-fluid method (Raeini et al., 2014; Ferrari et al., 2015) and level set method (Jettestuen et al., 2013). For a comprehensive review of these approaches, readers may refer to the articles by Golparvar et al. (2018) and Liu et al. (2016). Among these approaches, the LBM is becoming a popular choice for its simplicity and ability in modeling interfacial dynamics, dealing with complicated geometries, and parallel computing (Aidun and Clausen, 2010; Liu et al., 2016).

In this work, a recently-developed color-gradient lattice Boltzmann model, known as a quasi-three-dimensional (quasi-3D) model (Liu et al., 2021), is applied to simulate spontaneous imbibition through heterogeneous porous media micromodels. This quasi-3D model not only allows to wide range of viscosity ratios. More importantly, it only requires 2D computational cost while considering essential 3D effects. Thus, it is very suitable for the pore-scale simulation of spontaneous imbibition in micromodels where 3D effects must be involved account to overcome the capillary valve resistance (Liu et al., 2021). Nevertheless, some 3D effects such as wetting films and corner flows are not able to be captured by the quasi-3D simulation (Liu et al., 2021). In this sense, the quasi-3D simulation is actually a compromise solution to capture the 3D

effects. We first explore how the tortuosity influences the fluid distribution at breakthrough and the scaling relation between wetting fluid saturation and time for varying viscosity ratios, and then investigate the effect of mixed wettability on the fluid distribution, scaling exponent and the interface roughening.

2. Numerical method

2.1 A quasi-3D color-gradient LBM

Compared to the 3D model, the 2D model is preferred in pore-scale simulations for its advantage of low computational cost. However, when simulating spontaneous imbibition through a porous media micromodel, the 2D model is unable to capture some important flow phenomena such as the breakthrough of a capillary valve, due to the lack of capillary driving force in the depth direction. Fortunately, Liu et al. (2021) recently developed a quasi-3D color-gradient LBM that needs only 2D computational cost but considers essential 3D effects, and the capability and accuracy of this method were validated by the simulation of 3D capillary intrusion and capillary valve effect in a pore-throat structure, and by comparison with the micromodel experiment. Thus, the quasi-3D color-gradient LBM is applied to simulate spontaneous imbibition through heterogeneous micromodels in this study, and it is described as follows.

In this model, the distribution functions f_i^r and f_i^b are applied to represent the red (wetting) and blue (non-wetting) fluids, respectively. $f_i = f_i^r + f_i^b$ is the total distribution function, and the subscript i is the lattice velocity direction. The evolution of the distribution function consists of three steps, namely collision, recoloring and propagation. First, the collision step is implemented for the total distribution function, which reads as

$$f_i^{\dagger}(\mathbf{r},t) = f_i(\mathbf{r},t) + \Omega_i(\mathbf{r},t) + \overline{F_i}(\mathbf{r},t) \tag{1}$$

where f_i is the total distribution function in the ith velocity direction at the position $\mathbf{r}$ and time t, $f_i^{\dagger}$ is the post-collision distribution function, Ω_i is the collision term, and $\overline{F_i}$ is the forcing term.

To reduce spurious velocities near the interface and improve the numerical stability in simulation of two-phase flows with high viscosity ratio, the multiple-relaxation-time (MRT) collision term is adopted, which is given by (D'Humières et al., 2002)

$$\Omega_i(\mathbf{r},t) = -\sum_j (\mathbf{M}^{-1}\mathbf{S}\mathbf{M})_{ij}[f_j(\mathbf{r},t) - f_j^{eq}(\mathbf{r},t)] \tag{2}$$

where $\mathbf{M}$ is the transformation matrix, and $\mathbf{S}$ is the diagonal relaxation matrix. f_i^{eq} is the equilibrium distribution function defined by

$$f_i^{eq} = \rho\omega_i\left[1 + \frac{\mathbf{e}_i\cdot\mathbf{u}}{c_s^2} + \frac{(\mathbf{e}_i\cdot\mathbf{u})^2}{2c_s^4} - \frac{\mathbf{u}^2}{2c_s^2}\right] \tag{3}$$

where $\rho = \rho_r + \rho_b$ is the total density with the subscripts 'r' and 'b' referring to the red and blue fluids, respectively. $\mathbf{u}$ is the depth-averaged velocity, c_s is the speed of sound, $\mathbf{e}_i$ is the lattice velocity in the i direction, and ω_i is the weighting coefficient corresponding to the ith lattice velocity.

For the two-dimensional nine-velocity (D2Q9) model applied in the present LBM, the lattice velocities $\mathbf{e}_i$ and the weighting coefficients are given by

$$[\mathbf{e}_0,\mathbf{e}_1,...,\mathbf{e}_8] = \begin{pmatrix} 0 & 1 & 0 & -1 & 0 & 1 & -1 & -1 & 1 \\ 0 & 0 & 1 & 0 & -1 & 1 & 1 & -1 & -1 \end{pmatrix} \tag{4}$$

and

$$\omega_i = \begin{cases} 4/9, & i=0 \\ 1/9, & i=1,2,3,4 \\ 1/36, & i=5,6,7,8 \end{cases} \tag{5}$$

respectively. The speed of sound c_s is defined as

$$c_s = \frac{\delta_x}{\sqrt{3}\delta_t} \tag{6}$$

where δ_x and δ_t are the discrete steps in space and time, respectively, and they are both taken as 1 in this work. The transformation matrix $\mathbf{M}$ is explicitly given as (Krüger et al., 2017)

$$\mathbf{M} = \begin{pmatrix} 1 & 1 & 1 & 1 & 1 & 1 & 1 & 1 & 1 \\ -4 & -1 & -1 & -1 & -1 & 2 & 2 & 2 & 2 \\ 4 & -2 & -2 & -2 & -2 & 1 & 1 & 1 & 1 \\ 0 & 1 & 0 & -1 & 0 & 1 & -1 & -1 & 1 \\ 0 & -2 & 0 & 2 & 0 & 1 & -1 & -1 & 1 \\ 0 & 0 & 1 & 0 & -1 & 1 & 1 & -1 & -1 \\ 0 & 0 & -2 & 0 & 2 & 1 & 1 & -1 & -1 \\ 0 & 1 & -1 & 1 & -1 & 0 & 0 & 0 & 0 \\ 0 & 0 & 0 & 0 & 0 & 1 & -1 & 1 & -1 \end{pmatrix} \tag{7}$$

and the diagonal relaxation matrix $\mathbf{S}$ reads as

$$\mathbf{S} = \mathrm{diag}(0, s_v, s_v, 0, s_q, 0, s_q, s_v, s_v) \tag{8}$$

where

$$s_v = \frac{1}{3\nu + 0.5},\ s_q = \frac{8(2-s_v)}{8-s_v} \tag{9}$$

ν is the kinematic viscosity of fluid mixture and it is calculated as

$$\frac{1}{\nu} = \frac{1+\rho^N}{2\nu_r} + \frac{1-\rho^N}{2\nu_b} \tag{10}$$

where ν_r and ν_b are the kinematic viscosities of pure red and blue fluids, respectively. ρ^N is the color function used to distinguish different fluids, which is defined by

$$\rho^N(\mathbf{r}) = \frac{\rho_r(\mathbf{r}) - \rho_b(\mathbf{r})}{\rho_r(\mathbf{r}) + \rho_b(\mathbf{r})} \tag{11}$$

It can be seen from the above equation that the fluid is identified as red for $\rho^N = 1$ and as blue for $\rho^N = -1$; the fluid is a mixture of both red and blue fluids, namely the interface for $-1 < \rho^N < 1$.

In the quasi-3D model, the depth effect needs to be properly considered: (1) the frictional resistances from the top

and bottom walls, and (2) the additional interface curvature in the depth direction. For a creeping flow, the effect of viscosity can be realized by adding the term $-(\rho v/K_\varepsilon)\mathbf{u}$, to the momentum equations, where K_ε is the equivalent permeability defined by the micromodel depth h as $K_\varepsilon = -h^2/12$ (Horgue et al., 2013). Through the depth h and the contact angle θ, the additional interface curvature can be analytically expressed as $-2\cos\theta/h$ (Yin et al., 2019). Consequently, the local interface curvature κ_ε, as the sum of the curvatures in the computational $(x-y)$ plane and in the depth (z) direction, is given by

$$\kappa_\varepsilon = -\nabla s\cdot\mathbf{n} - \frac{2\cos\theta}{h} \tag{12}$$

where $\mathbf{n} = \nabla\rho^N/|\nabla\rho^N|$ is the unit interface normal vector in $x-y$ plane, and $\nabla s = \nabla - \mathbf{n}(\mathbf{n}\cdot\nabla)$ is the surface gradient operator. Using the continuum surface force model, the capillary force $\mathbf{F}_{IT}$ is proportional to the local interface curvature κ_ε, and is given by (Lishchuk et al., 2003)

$$\mathbf{F}_{IT} = \frac{1}{2}\sigma\kappa_\varepsilon\nabla\rho^N \tag{13}$$

where σ is an interfacial tension parameter.

To account for the additional viscosity effect and generate the capillary force at the interface, the forcing term $\overline{F_i}$ in Eq. (1) reads as

$$\overline{\mathbf{F}} = \mathbf{M}^{-1}\left(\mathbf{I} - \frac{1}{2}\mathbf{S}\right)\mathbf{M}\widetilde{\mathbf{F}} \tag{14}$$

where $\mathbf{I}$ is the unit matrix, and $\widetilde{\mathbf{F}}=[\widetilde{F}_0,\widetilde{F}_1,\widetilde{F}_2,...,\widetilde{F}_8]^T$ with $\widetilde{F}_i$ defined by (Guo et al., 2002)

$$\widetilde{F}_i = \omega_i\left[\frac{\mathbf{e}_i-\mathbf{u}}{c_s^2} + \frac{(\mathbf{e}_i-\mathbf{u})\mathbf{e}_i}{c_s^4}\right]\cdot\left(\mathbf{F}_{IT} - \frac{\rho v}{K_\varepsilon}\mathbf{u}\right) \tag{15}$$

Accordingly, the depth-averaged velocity can be computed by (Liu et al., 2021)

$$\mathbf{u}(\mathbf{r},t) = \frac{\sum_i f_i(\mathbf{r},t)\mathbf{e}_i + \frac{1}{2}\mathbf{F}_{IT}(\mathbf{r},t)}{\rho + \frac{\rho v}{2K_\varepsilon}} \tag{16}$$

After the collision step, a recoloring step is applied in order to guarantee the immiscibility of both fluids and obtain a reasonable diffuse interface. The recolored distribution functions are given as (Latva-Kokko and Rothman, 2005)

$$\begin{aligned} f_i^{r\dagger\dagger}(\mathbf{r},t) &= \frac{\rho_r}{\rho}f_i^{\dagger}(\mathbf{r},t) + \beta\frac{\rho_r\rho_b}{\rho}\omega_i\cos(\varphi_i)|\mathbf{e}_i| \\ f_i^{b\dagger\dagger}(\mathbf{r},t) &= \frac{\rho_b}{\rho}f_i^{\dagger}(\mathbf{r},t) + \beta\frac{\rho_r\rho_b}{\rho}\omega_i\cos(\varphi_i)|\mathbf{e}_i| \end{aligned} \tag{17}$$

where $f_i^{r\dagger\dagger}$ and $f_i^{b\dagger\dagger}$ are the recolored distribution functions of the red and blue fluids, respectively. β is the segregation parameter, which is set to 0.7 for numerical stability and accuracy. φ_i is the angle between the color gradient and the lattice velocity $\mathbf{e}_i$, and it is given by

$$\cos(\varphi_i) = \frac{\mathbf{e}_i\cdot\nabla\rho^N}{|\mathbf{e}_i||\nabla\rho^N|} \tag{18}$$

Finally, both red and blue distribution functions stream to the neighboring lattice nodes along the lattice velocity direction in the propagation step, which reads as

$$f_i^{\alpha}(\mathbf{r}+\mathbf{e}_i,t+1) = f_i^{\alpha\dagger\dagger}(\mathbf{r},t),\ \ \alpha = r \text{ or } b \tag{19}$$

The resulting distribution functions allow us to compute the local densities of red and blue fluids through

$$\rho_a(\mathbf{r},t) = \sum_i f_i^{\alpha}(\mathbf{r},t),\ \ \alpha = r \text{ or } b \tag{20}$$

2.2 Boundary conditions

We consider a micromodel initially filled saturated with the non-wetting fluid, which has an inlet at the upper boundary ($y = y_{\max}$) and an outlet at the lower boundary ($y = 0$). It is assumed that the wetting fluid spontaneously imbibes into the micromodel from the inlet and expels the non-wetting fluid out from the outlet. To achieve this, the modified periodic boundary conditions are applied at the inlet and outlet (Liu et al., 2021)

$$\begin{aligned} f_i^r[(x,y_{\max}),t+1] &= f_i^{b\dagger\dagger}[(x-e_{ix},0),t] \\ f_i^b[(x,y_{\max}),t+1] &= f_i^{r\dagger\dagger}[(x-e_{ix},0),t] \end{aligned} \quad i=4,7,8$$
$$\begin{aligned} f_i^r[(x,0),t+1] &= f_i^{b\dagger\dagger}[(x-e_{ix},y_{\max}),t] \\ f_i^b[(x,0),t+1] &= f_i^{r\dagger\dagger}[(x-e_{ix},y_{\max}),t] \end{aligned} \quad i=2,5,6 \tag{21}$$

All boundaries except both inlet and outlet are set to solid surfaces. On the solid surfaces, we impose no-slip boundary conditions using the mid-grid bounce-back scheme (Ladd, 1994), and implement the contact angle through the wetting boundary condition proposed by Xu et al. (2017). The basic idea of the wetting boundary condition is to modify the direction of the color gradient $\nabla\rho^N$ at three-phase contact lines so as to match the desired contact angle θ. This wetting boundary condition has gained great success in pore-scale two-phase simulations (Xu and Liu, 2018; Gu et al., 2019, 2021; Liu et al., 2021), and its details can be found in Xu et al. (2017).

3. Spontaneous imbibition into heterogeneous micromodels

3.1 The effect of tortuosity

In order to investigate the effect of tortuosity on the spontaneous imbibition process, four heterogeneous micromodels with different pore structures are considered, which are shown in Fig. 1. Each micromodel has a size of 1426×1932 lu^2, where lu represents the lattice length unit. The void space consists of circular pores with the diameter of 75 lu and rectangular throats with the width of 28 lu. The pores and throats are randomly distributed in the micromodel, and some of them may be overlapped. The number of throats needs to vary with the tortuosity. Specifically, the number of longitudinal throats increases while of transverse throats decreases with the increase of the micromodel tortuosity. Unless otherwise stated, the micromodel depth is uniform and is fixed at $h = 10$ lu. In our LBM simulations, the dynamic viscosity of the

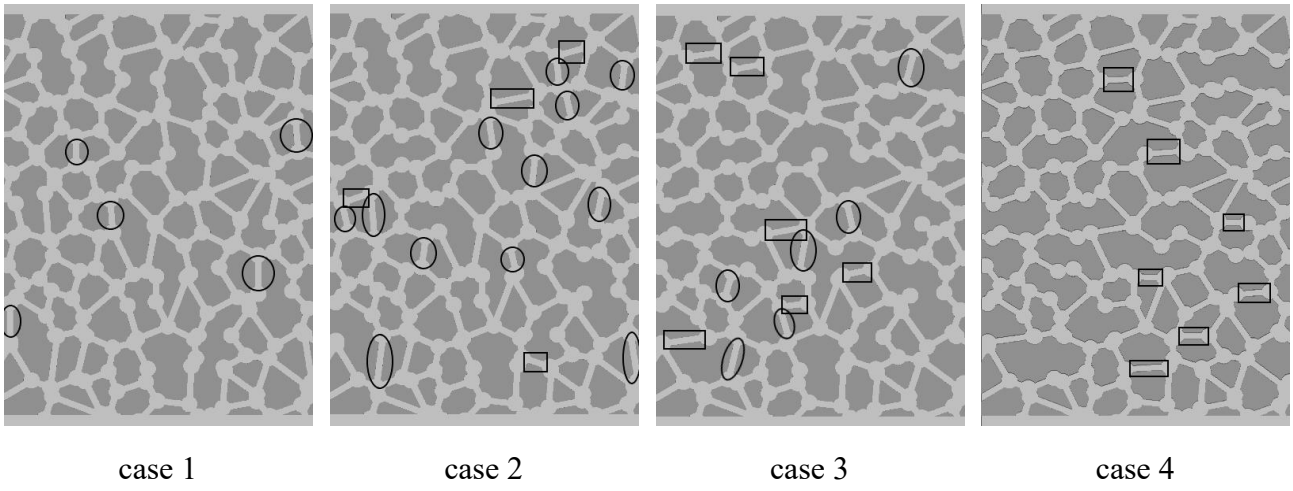

Fig. 1. Heterogeneous micromodels with roughly the same porosity but different tortuosities. Tortuosity increases from case 1 to case 4.

more viscous fluid, μ_{mv}, is fixed at 0.1, the interfacial tension $\sigma = 0.1$, and the grid size δ_x and time step δ_t are both taken as 1. To match these LBM simulation parameters, which are all presented in lattice units, to their physical values, three reference quantities have to be chosen: a length scale L_0, a time scale T_0, and a mass scale M_0. Here, we choose $L_0 = 5 \times 10^{-6}$ m, $T_0 = 2.5 \times 10^{-6}$ s and $M_0 = 1.25 \times 10^{-13}$ kg. A simulation parameter with dimensions $[\mathrm{m}]^{n1}[\mathrm{s}]^{n2}[\mathrm{kg}]^{n3}$ is multiplied by $[L_0]^{n1}[T_0]^{n2}[M_0]^{n3}$ to obtain the corresponding physical value. In this way, one can obtain the physical value of more viscous fluid viscosity μ_{mv}^{phy} by $\mu_{mv}^{phy} = \mu_{mv} \cdot M_0/(L_0 T_0) = 0.1 \cdot (1.25 \times 10^{-13})/[(5 \times 10^{-6}) \cdot (2.5 \times 10^{-6})] = 10^{-3}$ Pa·s, the physical value of interfacial tension σ^{phy} by $\sigma^{phy} = \sigma \cdot M_0/T_0^2 = 0.1 \cdot (1.25 \times 10^{-13})/(2.5 \times 10^{-6})^2 = 2 \times 10^{-3}$ N/m, the physical value of grid size δ_x^{phy} by $\delta_x^{phy} = \delta_x L_0 = 1 \cdot (5 \times 10^{-6}) = 5 \times 10^{-6}$ m, and the physical value of time step δ_t^{phy} by $\delta_t^{phy} = \delta_t L_0 = 1 \cdot (2.5 \times 10^{-6}) = 2.5 \times 10^{-6}$ s.

According to Nabovati and Sousa (2007), the micromodel tortuosity τ can be calculated in a single-phase Darcy flow by

$$\tau = \frac{\sum_{\mathbf{x}} \sqrt{u_x(\mathbf{x})^2 + u_y(\mathbf{x})^2}}{\sum_{\mathbf{x}} |u_y(\mathbf{x})|} \tag{22}$$

where u_x and u_y are the x-component and y-component of the velocity $\mathbf{u}$. Thus, we first simulate the single-phase flow in four different micromodels under the action of external force, and the obtained steady-state velocities are then used to calculate the tortuosities. Table 1 shows the physical parameters including permeability, porosity and tortuosity obtained from the single-phase flow simulations for four different cases, in which the permeability is normalized by the area of micromodel. It is seen that these cases are of roughly the same porosity. From case 1 to case 4, the permeability decreases monotonically while the tortuosity increases monotonically. In particular, the permeability decreases faster from case 2 to case 3.

We next investigate the imbibition behavior for three representative viscosity ratios, i.e., $\lambda = 0.02, 1$ and 50 at various tortuosities. The viscosity ratio is defined as the ratio of the wetting fluid viscosity to the non-wetting fluid viscosity, and

Table 1. Values of physical parameters for four different cases.

Parameters	case 1	case 2	case 3	case 4
Permeability	1.644	1.521	1.111	1.025
Porosity	0.424	0.424	0.416	0.415
Tortuosity	1.173	1.193	1.285	1.355

Notes: For these cases, the corresponding porous media micromodels are shown in Fig. 1. The permeability is normalized by the area of micromodel.

different viscosity ratios are obtained by varying the viscosity of less viscous fluid. A constant contact angle of $\theta = 50^\circ$ (measured from the wetting fluid side) is adopted, and each simulation is run until the wetting fluid breaks through the pore network. Fig. 2 presents the fluid distributions at breakthrough for different values of λ. For $\lambda = 0.02$, the injected wetting fluid bypasses a portion of the in-situ non-wetting fluid that it is trying to displace, so preferential flow paths or fingers of wetting fluid are clearly seen in the imbibition process, known as unstable displacement (Liu et al., 2021). It is also seen that unstable displacement changes slightly with the increase of tortuosity. This is because the unstable displacement generally develops from a few longitudinal throats. During the development of unstable displacement, the wetting fluid in a pore randomly flows into the neighboring throat connected to that pore. If the number of the longitudinal throats decreases or the number of the transverse throats increases, the wetting fluid that would have been imbibed into the longitudinal throats will randomly flow into the other transverse throats for further displacement due to the decrease in the number of longitudinal throats. In the cases of $\lambda = 1$ and $\lambda = 50$, the more viscous wetting fluid is imbibed into micromodel, resulting in the displacement of non-wetting fluid with a nearly flat front and thus leaving behind very little non-wetting fluid, which is known as the stable displacement (Lenormand et al., 1988). For such two viscosity ratios, the trapped non-wetting fluid overall increases in amount with the tortuosity. On one hand,

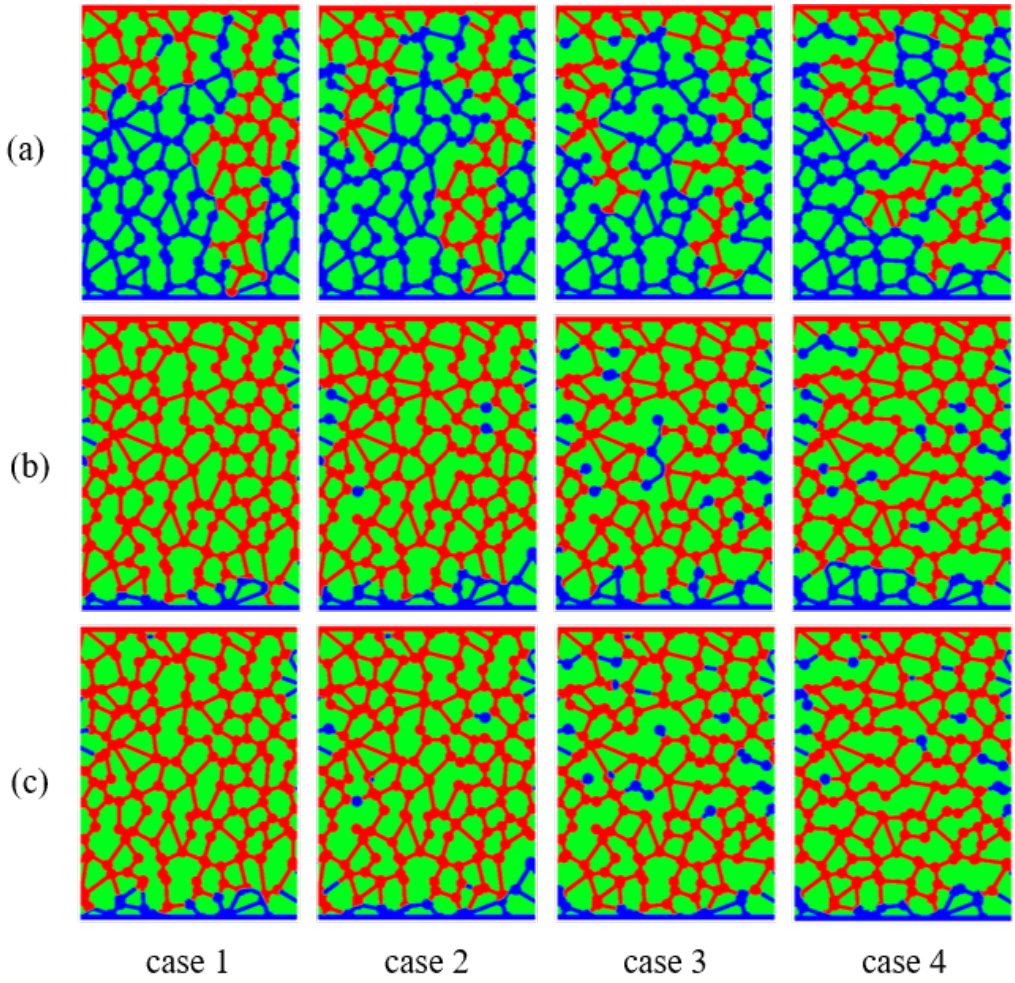

Fig. 2. Variation of the fluid distribution at breakthrough with the tortuosity for (a) $\lambda = 0.02$, (b) $\lambda = 1$ and (c) $\lambda = 50$. The wetting fluid, non-wetting fluid, and the solid are indicated in red, blue, and green, respectively. Note that the tortuosity increases gradually from case 1 to case 4.

the reduction in the number of longitudinal throats makes some pores connected only by transverse throats. The non-wetting fluid in such pores can merely be displaced by the wetting fluid imbibed from the left or right transverse throat. At this point, the non-wetting fluid may be trapped by the wetting fluid that simultaneously enters the left and right throats. On the other hand, with increasing the number of transverse throats, more wetting fluid is imbibed into the transverse throats, leading to an increased chance of being trapped for the non-wetting fluid.

The wetting fluid saturation S_w as a function of time for various tortuosities and viscosity ratios is shown in Fig. 3. By combining Fig. 3 and Table 1, it is seen that as the tortuosity increases, the micromodel permeability and the imbibition rate both decrease monotonously. Like the permeability, the imbibition rate also decreases more significantly from case 2 to case 3. Below, we can make a qualitative analysis to explain why the imbibition rate decreases with tortuosity. For the sake of simplicity, we assume $\lambda = 1$ in the analysis. According to Lucas-Washburn law (Lucas, 1918; Washburn, 1921), the theoretical solution of the imbibition length $l(t)$ can be derived by the balance between the capillary pressure and the viscous pressure drop, which reads as

$$l(t) = \frac{\sigma h \cos\theta}{6\rho v_w L_t} t + l_0 \tag{23}$$

where L_t is the total flow length of the wetting fluid during spontaneous imbibition, and l_0 is the imbibition length at the initial time ($t = 0$). Based on the definition of tortuosity, L_t can be related to the micromodel length L as $L_t = \tau L$. Obviously, L_t increases with τ, so the imbibition rate $(\sigma h \cos\theta)/(6\rho v_w L_t)$ decreases with increasing tortuosity. In addition, it can be observed that at $\lambda = 1$ and $\lambda = 50$, the wetting fluid saturation at breakthrough gradually reduces with increasing tortuosity, consistent with the previous analysis that the non-wetting fluid becomes more trapped as the tortuosity increases.

A number of studies (Family et al., 1992; Li and Horne, 2004; Bru and Pastor, 2006; Cai and Yu, 2011) showed that the wetting fluid saturation exhibits a power-law dependence on the time during the spontaneous imbibition, i.e.,

$$S(t) = at^b + S_0 \tag{24}$$

where S_0 is the initial saturation, and a and b are the fitting parameters. We also use Eq. (24) to fit our numerical results

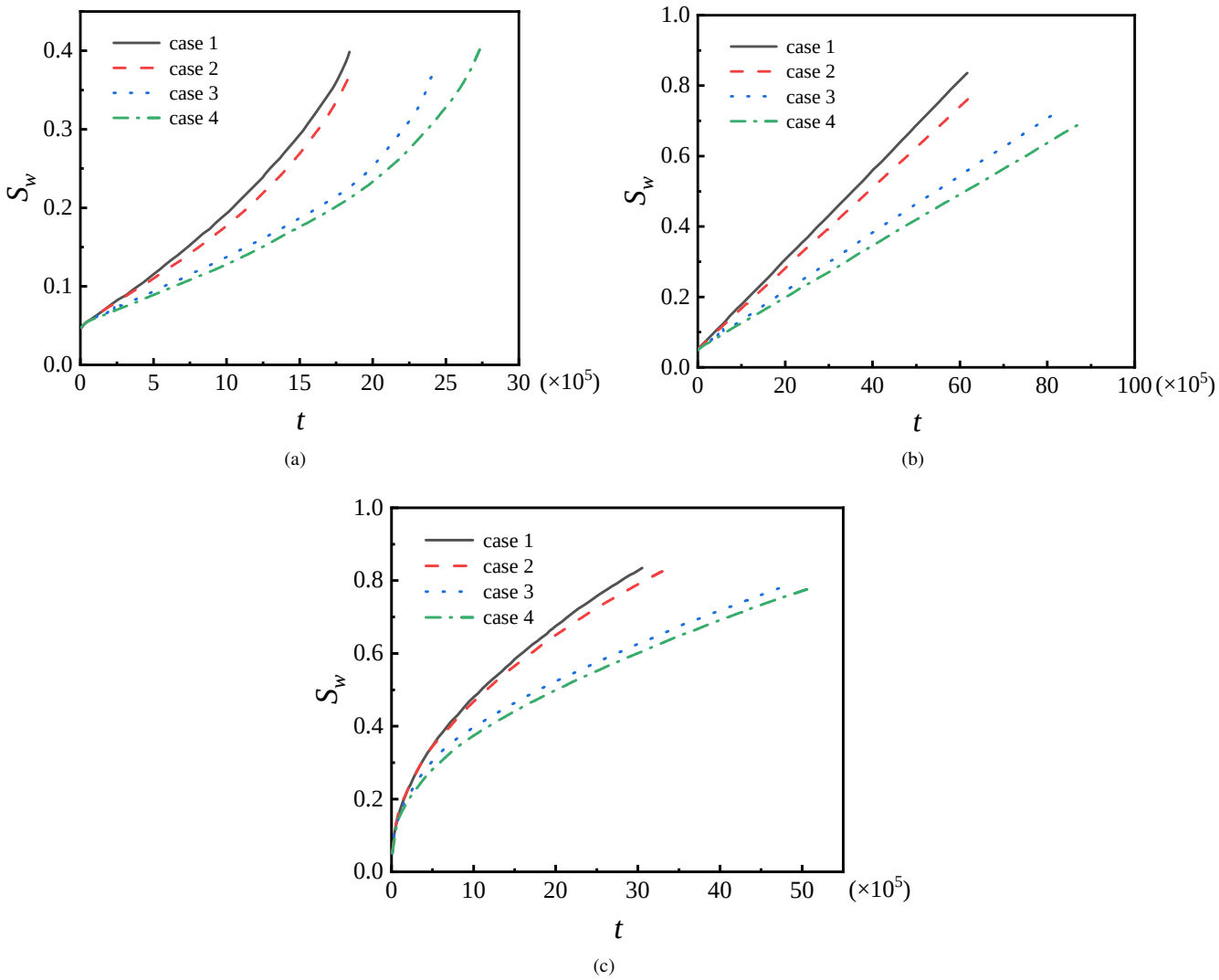

Fig. 3. Time evolution of the wetting fluid saturation for different tortuosities at (a) $\lambda = 0.02$, (b) $\lambda = 1$ and (c) $\lambda = 50$. Note that the time t is presented in lattice time unit, and each lattice time unit corresponds to the physical time of 2.5 μs.

and find all the results can be well described by this equation. Here, we explore how the scaling exponent b varies with the tortuosity for different viscosity ratios. Table 2 presents the fitted scaling exponents for different viscosity ratios and tortuosities. It can be seen that for $\lambda = 0.02$, the values of b are all greater than unity, and the exponent b increases with the tortuosity; for $\lambda = 1$, the values of b almost stabilize at 1, while the values of b fluctuate around 0.5 for $\lambda = 50$. We also notice that the variation of b with τ at $\lambda = 50$ is the same in trend as that at $\lambda = 1$. Specifically, the exponent b decreases with increasing τ from 1.173 to 1.285 (see cases 1 to 3), consistent with the previous finding by Cai and Yu (2011) in trend; however, b increases upon further increasing τ from 1.285 to 1.355 (see cases 3 to 4), which may be attributed to the following reasons. In Fig. 1, the throats circled by black circles are the longitudinal throats that are replaced by solids in the next case; the throats circled by black rectangles are the newly added transverse throats compared with the previous case. Specifically, from case 1 to case 2, 5 longitudinal throats are removed and 4 transverse throats are added; from case 2 to case 3, 12 longitudinal throats are removed and 6 transverse throats are added; from case 3 to case 4, 6 longitudinal throats

Table 2. Values of physical parameters for four different cases.

Viscosity ratio	case 1	case 2	case 3	case 4
0.02	1.424	1.526	1.655	1.773
1	1.004	0.996	0.989	0.993
50	0.536	0.511	0.484	0.510

Notes: For these cases, the corresponding porous media micromodels are shown in Fig. 1. The permeability is normalized by the area of micromodel.Values of fitted scaling exponent b for different viscosity ratios and cases. The value of b is obtained by using Eq. (24) to fit the numerical results. The viscosity ratio is defined as the ratio of the dynamic viscosity of the wetting fluid to that of the non-wetting fluid, and four different cases correspond to the porous media micromodels shown in Fig. 1.

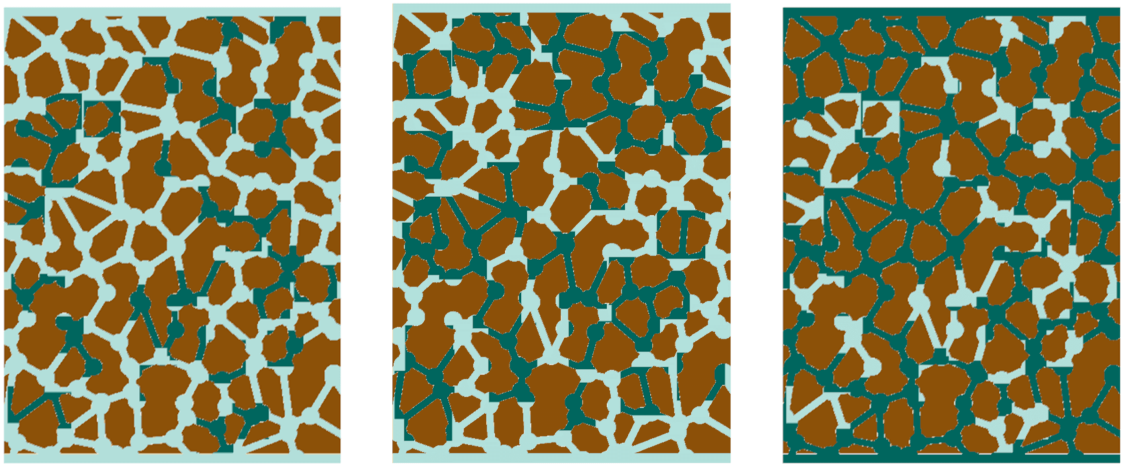

(a) (b) (c)

Fig. 4. Three different mixed wettabilities, which correspond to (a) SWH: 70% strongly wet region and 30% weakly wet region, (b) SWM: 50% strongly wet region and 50% weakly wet region, and (c) SWL: 30% strongly wet region and 70% weakly wet region. The solid, weakly wet region, and the strongly wet region are indicated in brown, dark green, and light green, respectively.

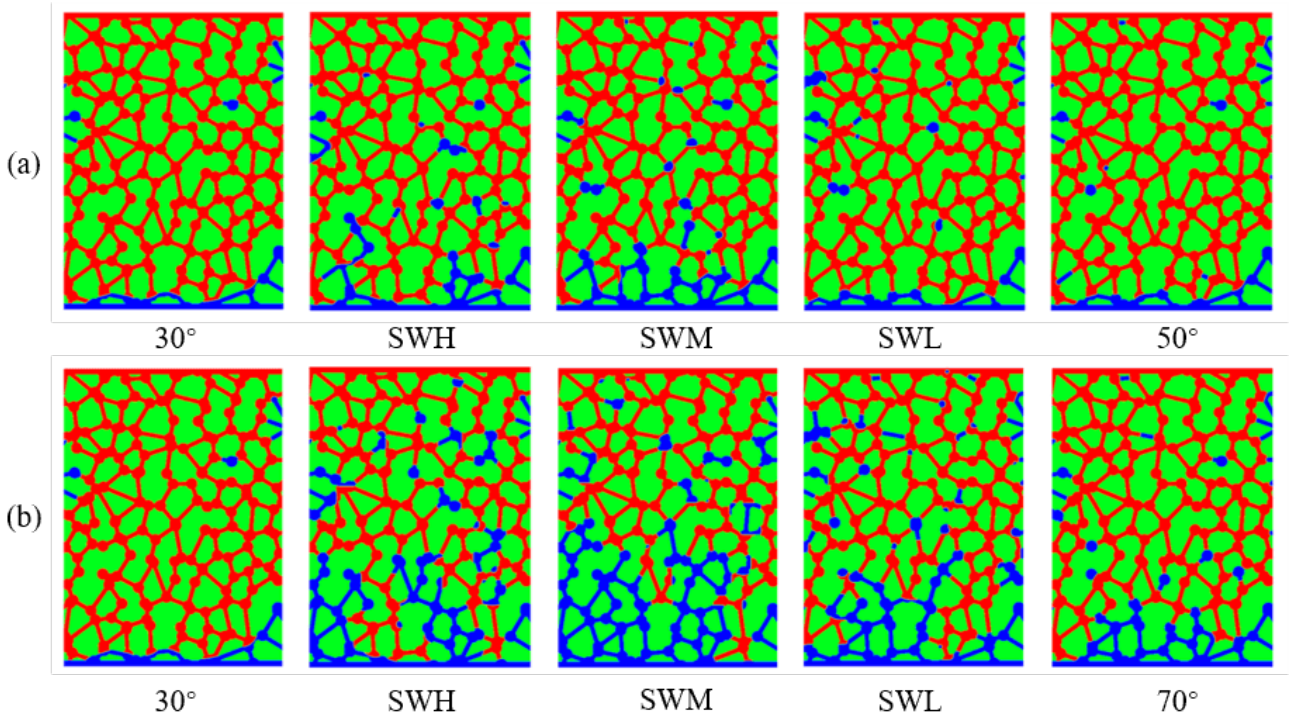

Fig. 5. Fluid distributions at breakthrough under different mixing degrees of wettabilities for (a) $\{\theta_S, \theta_W\} = \{30°, 50°\}$ and (b) $\{\theta_S, \theta_W\} = \{30°, 70°\}$. The wetting fluid, non-wetting fluid, and the solid are indicated in red, blue, and green, respectively.

are removed and 7 transverse throats are added. It is clear that the first two variations, i.e., from case 1 to case 2 and from case 2 to case 3, are that the reduction in the number of longitudinal throats is greater than the increase in the number of transverse throats, which is contrary to the third variation, i.e., from case 3 to case 4. This suggests that the scaling exponent may be also related to the variation of the longitudinal and transverse throats in addition to the variation in tortuosity. To be specific, the reduction of longitudinal throats results in the decrease of scaling exponent while the increase of transverse throats leads to the increase of scaling exponent.

3.2 The effect of mixed wettability

In this section, the influence of mixed wettability is investigated at $\lambda = 50$ for a specific micromodel geometry, i.e., the one used in the case 2 above. As shown in Fig. 4, we consider three different mixed wettabilities: (a) 70% strongly wet region and 30% weakly wet region, (b) 50% strongly wet region and 50% weakly wet region, and (c) 30% strongly wet region and 70% weakly wet region, which are named as SWH, SWM

and SWL, respectively. For the convenience of description, the contact angles in strongly and weakly wet regions are denoted as θ_S and θ_W, respectively.

Two groups of θ_S and θ_W are investigated, i.e., $\{\theta_S,\theta_W\}=\{30^\circ,50^\circ\}$ and $\{\theta_S,\theta_W\}=\{30^\circ,70^\circ\}$. For each group of θ_S and θ_W, we also consider the uniform wettability cases of $\theta=\theta_S$ and $\theta=\theta_W$ in addition to three mixed wettability cases. Fig. 5 shows the fluid distributions at breakthrough for (a) $\{\theta_S,\theta_W\}=\{30^\circ,50^\circ\}$ and (b) $\{\theta_S,\theta_W\}=\{30^\circ,70^\circ\}$. For the uniform wettabilities of $\theta=30^\circ$ and $\theta=50^\circ$, the displacement pattern exhibits a nearly flat front with very little trapping of non-wetting fluid , which is typical of stable displacement. As the contact angle θ rises to 70°, more non-wetting fluid would be trapped in the micromodel, and the roughness width of imbibition fronts increases significantly. In the mixed wettability cases, the blobs of non-wetting fluid trapped by the wetting fluid first increase and then decrease as the weakly wet fraction increases. This means that the higher the mixing degree of two wettabilities, the easier it is to generate the non-wetting fluid blobs, which results in less effective displacement. By comparing two groups of mixed wettability, it is shown that the number of non-wetting fluid blobs increases more significantly with the mixing degree, and the preferential flow paths tend to be formed, similar to those in the situation of $\lambda<1$. This is because when the contact angle θ_W increases to 70°, the capillary driving force from the wetting fluid is greatly reduced in weakly wet region, and thus the wetting fluid tends to imbibe into strongly wet region, forming preferential flow paths.

We also quantify the influence of mixed wettability on preferential flow paths through the roughness width at breakthrough for $\{\theta_S,\theta_W\}=\{30^\circ,70^\circ\}$. The roughness width W_f is defined as (Bakhshian et al., 2020)

$$W_f=\sqrt{\langle[h(x,t_b)-\widetilde{h}(t_b)]^2\rangle_x} \tag{25}$$

where $h(x,t_b)$ is the position of the front interface in the vertical direction at the horizontal position x and the breakthrough time t_b. $\widetilde{h}(t_b)=\langle h(x,t_b)\rangle_x$ with $\langle\cdot\rangle_x$ denoting the spatial average over all x in the horizontal direction. Fig. 6 depicts the roughness widths at breakthrough for different wetting conditions, in which the abscissa f_W represents the fraction of weakly wet region. As can be seen from Fig. 6, the minimum roughness width occurs at $\theta=30^\circ$ ($f_W=0$), and its value is close to 0, indicating that the imbibition fronts in this case are almost flat and there is no preferential flow path. When θ increases to 70° ($f_W=1$), the fronts are significantly roughened with the roughness width up to nearly 140 lu (i.e., 700 μm), and the preferential flow paths appear. This indicates that the reduced surface wettability is favorable to the roughening of interfaces in uniform wettability condition. This is because when the micromodel surface becomes less wetting, the resistance caused by capillary valve effect, defined by the throat width w as $-\sigma\sin\theta/w$ (Xu et al., 2017), is enhanced, and the displacement process is more dependent on the specific pore-throat structure of the micromodel. In the mixed wettability condition, the values of roughness width for both SWH ($f_W=0.3$) and SWL ($f_W=0.7$) approximately

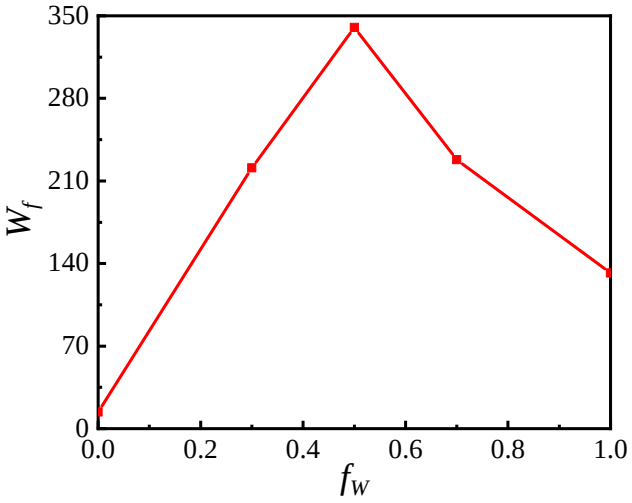

Fig. 6. The roughness width at breakthrough as a function of the weakly wet fraction f_W for $\{\theta_S,\theta_W\}=\{30^\circ,70^\circ\}$. Note that the roughness width W_f is presented in lattice length unit (lu), and each lattice length unit corresponds to the physical length of 5 μm.

equal 220 lu (i.e., 1100 μm), which is much lower than that for SWM ($f_W=0.5$). In addition, we notice in Fig. 6 that the roughness width in mixed wettability condition is always greater than that in uniform wettability condition, which suggests that the mixed wettability also favors the interface roughening. This can be explained as follows: in the mixed wettability condition, especially when the difference between θ_S and θ_W is large, the displacement preferentially occurs in strongly wet region, and it would not proceed in weakly wet region until completing the preferential displacement in strongly wet region. This is equivalent to that the connectivity of a micromodel is greatly reduced during the displacement process, which results in the intensification of interface roughening.

Furthermore, we find that our data in the mixed wettability condition can be perfectly described by Eq. (24), but we are not sure if the scaling exponent $b=0.5$, as described by the LW equation. To clarify this, Fig. 7 plots the wetting fluid saturation S_w as a function of $\sqrt{t}$ for $\{\theta_S,\theta_W\}=\{30^\circ,50^\circ\}$ and $\{\theta_S,\theta_W\}=\{30^\circ,70^\circ\}$. For $\sqrt{t}$ for $\{\theta_S,\theta_W\}=\{30^\circ,50^\circ\}$, the linear relations are clearly seen for different mixing degrees in the $S_w-\sqrt{t}$ plot, suggesting that the LW equation can be satisfied; whereas for $\{\theta_S,\theta_W\}=\{30^\circ,70^\circ\}$, the results deviate from the linear relation in mixed wettability condition, meaning that the LW equation is no longer valid. We also fit the simulation data to obtain the scaling exponents, and the results are shown in Table 3. It can be observed that the relative error of b, which is defined as $E=(|0.5-b|/0.5)\times100\%$, in the mixed wettability condition is limited to no more than 6% for $\{\theta_S,\theta_W\}=\{30^\circ,50^\circ\}$. By contrast, for $\{\theta_S,\theta_W\}=\{30^\circ,70^\circ\}$, the relative error E in the mixed wettability condition ranges from 13% to 26.8%, which correspond to SWL ($f_W=0.7$) and SWM ($f_W=0.5$), respectively. Again, these results indicate that the LW equation is not suitable for spontaneous imbibition in a micromodel with large wettability difference. In addition, as seen from the insets in Fig. 7, in mixed wettability condi-

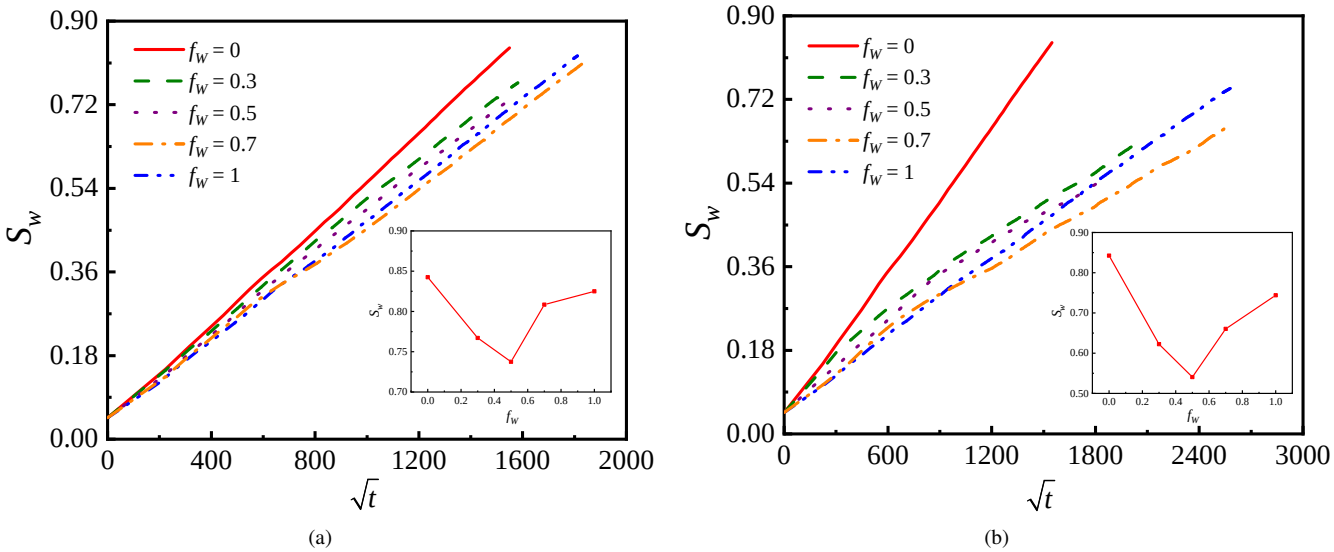

Fig. 7. The wetting fluid saturation S_w versus $\sqrt{t}$ under different mixing degrees of wettabilities for (a) $\{\theta_S, \theta_W\} = \{30°, 50°\}$ and (b) $\{\theta_S, \theta_W\} = \{30°, 70°\}$. The insets are included to show how the wetting fluid saturation at breakthrough varies with the mixing degree f_W. Note that the time t is presented in lattice time unit, and each lattice time unit corresponds to the physical time of 2.5 μs.

Table 3. Values of fitted scaling exponent b under different mixing degrees of wettabilities for $\sqrt{t}$ for $\{\theta_S, \theta_W\} = \{30°, 50°\}$ and $\{\theta_S, \theta_W\} = \{30°, 70°\}$. f_W represents the fraction of weakly wet region, and the value of b is obtained by using Eq. (24) to fit the numerical results.

f_W	b	
	$\{\theta_S, \theta_W\}$={30°, 50°}	$\{\theta_S, \theta_W\}$={30°, 70°}
0.0	0.5164	0.5164
0.3	0.4701	0.3842
0.5	0.4769	0.3661
0.7	0.5173	0.4352
1.0	0.5114	0.4822

tion, the wetting fluid saturation at breakthrough is lower than that in uniform wettability condition, and its value decreases with increasing the mixing degree of two wettabilities. This also indirectly explains why the connectivity of the micromodel is reduced in mixed wettability condition.

Finally, we also notice an interesting phenomenon in Fig. 7. In mixed wettability condition, the imbibition rate is higher in the early stage, and then gradually decreases and becomes lower than that in the uniform wettability condition with high θ ($f_W = 1$). Such a late-stage behavior seems counterintuitive and is contrary to the prediction of LW equation, from which the uniform wettability condition with high θ should correspond to the weakest displacement capability and thus to the slowest displacement rate. This can be explained as follows: In mixed wettability condition, the wetting fluid preferentially invades strongly wet region, reducing the connectivity of the micromodel and leading to the formation of preferential flow paths. As a result, fewer live fronts are exposed to the pores and throats, which decreases the driving force for spontaneous imbibition and thus the imbibition rate.

4. Conclusions

In this work, a quasi-3D color-gradient LBM, recently developed by Liu et al. (2021) is applied to simulate the spontaneous imbibition in heterogeneous porous media micromodels, where the influence of tortuosity and mixed wettability is investigated. The results show that for various tortuosities, the unstable displacement occurs at $\lambda < 1$ and the stable displacement occurs at $\lambda \geq 1$. For the stable displacement, the trapped blobs of non-wetting fluid increase in amount as the tortuosity increases. By establishing the power-law relationship between wetting fluid saturation and time, it is found that as the tortuosity grows, the scaling exponent b gradually increases when $\lambda < 1$ but overall presents a decreasing trend when $\lambda \geq 1$. In addition, the findings also reveal that b is not only affected by tortuosity, but also related to the pore throat structure of the micromodel. For different mixed wettabilities at a favorable viscosity ratio ($\lambda = 50$), the results indicate that in the mixed wettability condition of $\theta_S = 30°$ and $\theta_W = 70°$, unstable displacement is clearly seen, which depends on the mixing degree of two wettabilities. To be specific, the greater the mixing degree, the more unstable the displacement will become; accordingly, the wetting fluid saturation at breakthrough is lower. The power-law relationship between wetting fluid saturation and time deviates significantly from the LW equation when unstable displacement occurs. Due to the reduction in the connectivity of micromodel, it is observed that the wetting fluid imbibition rate in mixed wettability condition is lower than that in uniform wettability condition with $\theta = \theta_W$, although the latter correspond to a slow displacement according to the LW equation.

Acknowledgement

This work is supported by the National Natural Science Foundation of China (Nos. 51876170, 12072257), the National Key Project (No. GJXM92579) and the Natural Science Basic Research Plan in Shaanxi Province of China (No. 2019JM-343).

Conflict of interest

The authors declare no competing interest.

References

Ahmadi, S., Hosseini, M., Tangestani, E., et al. Wettability alteration and oil recovery by spontaneous imbibition of smart water and surfactants into carbonates. Petroleum Science, 2020, 17(3): 712-721.

Aidun, C. K., Clausen, J. R. Lattice-Boltzmann method for complex flows. Annual Review of Fluid Mechanics, 2010, 42: 439-472.

Andersen, P. O., Nesvik, E. K., Standnes, D. C. Analytical solutions for forced and spontaneous imbibition accounting for viscous coupling. Journal of Petroleum Science and Engineering, 2020, 186: 106717.

Bakhshian, S., Murakami, M., Hosseini, S. A., et al. Scaling of imbibition front dynamics in heterogeneous porous media. Geophysical Research Letters, 2020, 47(14): e2020GL087914.

Bandara, U. C., Tartakovsky, A. M., Oostrom, M., et al. Smoothed particle hydrodynamics pore-scale simulations of unstable immiscible flow in porous media. Advances in Water Resources, 2013, 62: 356-369.

Bartels, W. B., Rucker, M., Boone, M., et al. Imaging spontaneous imbibition in full Darcy-scale samples at pore-scale resolution by fast X-ray tomography. Water Resources Research, 2019, 55(8): 7072-7085.

Bru, A., Pastor, J. M. Experimental characterization of hydration and pinning in bentonite clay, a swelling, heterogeneous, porous medium. Geoderma, 2006, 134(3-4): 295-305.

Cai, J. C., Hu, X. Y., Standnes, D. C., et al. An analytical model for spontaneous imbibition in fractal porous media including gravity. Colloids and Surfaces A: Physicochemical and Engineering Aspects, 2012, 414: 228-233.

Cai, J. C., Yu, B. M. A discussion of the effect of tortuosity on the capillary imbibition in porous media. Transport in Porous Media, 2011, 89(2): 251-263.

Cai, J. C., Yu, B. M., Mei, M. F., et al. Capillary rise in a single tortuous capillary. Chinese Physics Letters, 2010, 27(5): 054701.

Chang, S., Seo, J., Hong, S., et al. Dynamics of liquid imbibition through paper with intra-fibre pores. Journal of Fluid Mechanics, 2018, 845: 36-50.

D'Humières, D., Ginzburg, I., Krafczyk, M., et al. Multiple-relaxation-time lattice Boltzmann models in three dimensions. Philosophical Transactions of the Royal Society A-Mathematical Physical and Engineering Sciences, 2002, 360(1792): 437-451.

Elizalde, E., Urteaga, R., Berli, C. L. A. Rational design of capillary-driven flows for paper-based microfluidics. Lab on a Chip, 2015, 15(10): 2173-2180.

Espin, L., Kumar, S. Droplet spreading and absorption on rough, permeable substrates. Journal of Fluid Mechanics, 2015, 784: 465-486.

Family, F., Chan, K. C. B., Amar, J. G., et al. Surface Disordering: Growth, Roughening and Phase Transitions. New York, USA, Nova Science, 1992.

Ferrari, A., Jimenez-Martinez, J., Le Borgne, T., et al. Challenges in modeling unstable two-phase flow experiments in porous micromodels. Water Resources Research, 2015, 51(3): 1381-1400.

Gao, L. H., Yang, Z. M., Shi, Y. Experimental study on spontaneous imbibition characteristics of tight rocks. Advances in Geo-Energy Research, 2018, 2(3): 292-304.

Gao, Z. Y., Hu, Q. H. Initial water saturation and imbibitibn fluid affect spontaneous imbibition into Barnett shale samples. Journal of Natural Gas Science and Engineering, 2016, 34: 541-551.

Gao, Z. Y., Hu, Q. H. Pore structure and spontaneous imbibition characteristics of marine and continental shales in China. AAPG Bulletin, 2018, 102(10): 1941-1961.

Gao, Z. Y., Yang, X. B., Hu, C. H., et al. Characterizing the pore structure of low permeability Eocene Liushagang Formation reservoir rocks from Beibuwan Basin in northern South China Sea. Marine and Petroleum Geology, 2019, 99: 107-121.

Golparvar, A., Zhou, Y., Wu, K., et al. A comprehensive review of pore scale modeling methodologies for multiphase flow in porous media. Advances in Geo-Energy Research, 2018, 2(4): 418-440.

Gruener, S., Huber, P. Imbibition in mesoporous silica: Rheological concepts and experiments on water and a liquid crystal. Journal of Physics: Condensed Matter, 2011, 23(18): 184109.

Gruener, S., Sadjadi, Z., Hermes, H. E., et al. Anomalous front broadening during spontaneous imbibition in a matrix with elongated pores. Proceedings of the National Academy of Sciences of the United States of America, 2012, 109(26): 10245-10250.

Gu, Q. Q., Liu, H. H., Wu, L. Preferential imbibition in a dual-permeability pore network. Journal of Fluid Mechanics, 2021, 915: A138.

Gu, Q. Q., Zhu, L. H., Zhang, Y. H., et al. Pore-scale study of counter-current imbibition in strongly water-wet fractured porous media using lattice Boltzmann method. Physics of Fluids, 2019, 31(8): 086602.

Guo, B., Bandilla, K. W., Nordbotten, J. M., et al. A multiscale multilayer vertically integrated model with vertical dynamics for CO_2 sequestration in layered geological formations. Water Resources Research, 2016, 52(8): 6490-6505.

Guo, Z. L., Zheng, C. G., Shi, B. C. Discrete lattice effects on the forcing term in the lattice Boltzmann method. Physical Review E, 2002, 65(4): 046308.

Horgue, P., Augier, F., Duru, P., et al. Experimental and numerical study of two-phase flows in arrays of cylinders. Chemical Engineering Science, 2013, 102: 335-345.

Hu, Q. H., Ewing, R. P., Dultz, S. Low pore connectivity in natural rock. Journal of Contaminant Hydrology, 2012, 133: 76-83.

Jettestuen, E., Helland, J. O., Prodanovic, M. A level set method for simulating capillary-controlled displacements at the pore scale with nonzero contact angles. Water Resources Research, 2013, 49(8): 4645-4661.

Joekar-Niasar, V., Hassanizadeh, S. M. Analysis of fundamentals of two-phase flow in porous media using dynamic pore-network models: A review. Critical Reviews in Environmental Science and Technology, 2012, 42(18): 1895-1976.

Karoglou, M., Moropoulou, A., Giakoumaki, A., et al. Capillary rise kinetics of some building materials. Journal of Colloid and Interface Science, 2005, 284(1): 260-264.

Krüger, T., Kusumaatmaja, H., Kuzmin, A., et al. The Lattice Boltzmann Method: Principles and Practice. Switzerland, Springer International Publishing, 2017.

Ladd, A. J. C. Numerical simulations of particulate suspensions via a discretized Boltzmann equation. Part 1. Theoretical foundation. Journal of Fluid Mechanics, 1994, 271: 285-309.

Latva-Kokko, M., Rothman, D. H. Diffusion properties of gradient-based lattice Boltzmann models of immiscible fluids. Physical Review E, 2005, 71(5): 056702.

Lenormand, R., Touboul, E., Zarcone, C. Numerical-models and experiments on immiscible displacements in porous-media. Journal of Fluid Mechanics, 1988, 189: 165-187.

Li, K., Horne, R. N. An analytical scaling method for spontaneous imbibition in gas/water/rock systems. SPE Journal, 2004, 9(3): 322-329.

Li, Y. L., Yu, D., Niu, B. L. Prediction of spontaneous imbibition in fractal porous media based on modified porosity correlation. Capillarity, 2021, 4(1): 13-22.

Lishchuk, S. V., Care, C. M., Halliday, I. Lattice Boltzmann algorithm for surface tension with greatly reduced microcurrents. Physical Review E, 2003, 67(3): 036701.

Liu, H. H., Kang, Q. J., Leonardi, C. R., et al. Multiphase lattice Boltzmann simulations for porous media applications. Computational Geosciences, 2016, 20(4): 777-805.

Liu, H. H., Sun, S. L., Wu, R., et al. Pore-scale modeling of spontaneous imbibition in porous media using the lattice Boltzmann method. Water Resources Research, 2021, 57: e2020WR029219.

Liu, J. R., Shen, J. J., Wang, X. K., et al. Experimental study of wettability alteration and spontaneous imbibition in Chinese shale oil reservoirs using anionic and nonionic surfactants. Journal of Petroleum Science and Engineering, 2019, 175: 624-633.

Liu, K. Q., Ostadhassan, M., Zou, J., et al. Multifractal analysis of gas adsorption isotherms for pore structure characterization of the Bakken Shale. Fuel, 2018, 219: 296-311.

Liu, Q., Song, R., Liu, J. J., et al. Pore-scale visualization and quantitative analysis of the spontaneous imbibition based on experiments and micro-CT technology in low-permeability mixed-wettability rock. Energy Science & Engineering, 2020, 8(5): 1840-1856.

Lucas, R. The time law of the capillary rise of liquids. Kolloid-Zeitschrift, 1918, 23(1): 15-22.

Nabovati, A., Sousa, A. C. M. Fluid flow simulation in random porous media at pore level using lattice Boltzmann method, in New Trends in Fluid Mechanics Research, edited by F. G. Zhuang and J. C. Li, Springer, Berlin, Heidelberg, pp. 518-521, 2007.

Raeini, A. Q., Blunt, M. J., Bijeljic, B. Direct simulations of two-phase flow on micro-CT images of porous media and upscaling of pore-scale forces. Advances in Water Resources, 2014, 74: 116-126.

Shi, H., Luo, X. R., Li, X., et al. Effects of mix-wet porous mediums on gas flowing and one mechanism for gas migration. Journal of Petroleum Science and Engineering, 2017, 152: 60-66.

Tartakovsky, A. M., Trask, N., Pan, K., et al. Smoothed particle hydrodynamics and its applications for multiphase flow and reactive transport in porous media. Computational Geosciences, 2016, 20(4): 807-834.

Wang, F. Y., Cheng, H. Effect of gravity on spontaneous imbibition of the wetting phase into gas-saturated tortuous fractured porous media: Analytical solution and diagnostic plot. Advances in Water Resources, 2020, 142: 103657.

Wang, L., He, Y. M., Xiao, Y. H., et al. Spontaneous gas-water imbibition in mixed-wet pores. Petrophysics, 2020, 61(2): 230-238.

Washburn, E. W. The dynamics of capillary flow. Physical Review, 1921, 17(3): 273-283.

Wijshoff, H. Drop dynamics in the inkjet printing process. Current Opinion in Colloid & Interface Science, 2018, 36: 20-27.

Xu, M., Liu, H. H. Prediction of immiscible two-phase flow properties in a two-dimensional Berea sandstone using the pore-scale lattice Boltzmann simulation. European Physical Journal E, 2018, 41(10): 124.

Xu, Z. Y., Liu, H. H., Valocchi, A. J. Lattice Boltzmann simulation of immiscible two-phase flow with capillary valve effect in porous media. Water Resources Research, 2017, 53(5): 3770-3790.

Yang, L., Ge, H. K., Shi, X., et al. The effect of microstructure and rock mineralogy on water imbibition characteristics in tight reservoirs. Journal of Natural Gas Science and Engineering, 2016, 34: 1461-1471.

Yin, X., Zarikos, I., Karadimitriou, N. K., et al. Direct simulations of two-phase flow experiments of different geometry complexities using Volume-of-Fluid (VOF) method. Chemical Engineering Science, 2019, 195: 820-827.

You, Q., Wang, H., Zhang, Y., et al. Experimental study on spontaneous imbibition of recycled fracturing flowback fluid to enhance oil recovery in low permeability

sandstone reservoirs. Journal of Petroleum Science and Engineering, 2018, 166: 375-380.

Zacharoudiou, I., Chapman, E. M., Boek, E. S., et al. Pore-filling events in single junction micro-models with corresponding lattice Boltzmann simulations. Journal of Fluid Mechanics, 2017, 824: 550-573.

Zheng, J. T., Chen, Z. Q., Xie, C. Y., et al. Characterization of spontaneous imbibition dynamics in irregular channels by mesoscopic modeling. Computers & Fluids, 2018, 168: 21-31.

Zhu, P., Dong, Y. X., Chen, M., et al. Quantitative evaluation of pore structure from mineralogical and diagenetic information extracted from well logs in tight sandstone reservoirs. Journal of Natural Gas Science and Engineering, 2020, 80: 103376.